Draft version November 29, 2016
Preprint typeset using LaTeX style emulateapj v. 5/2/11

arXiv:1611.08607v1 [astro-ph.GA] 25 Nov 2016

THERMODYNAMICS AND CHARGING OF INTERSTELLAR IRON NANOPARTICLES

Brandon S. Hensley
Jet Propulsion Laboratory, California Institute of Technology, 4800 Oak Grove Drive, Pasadena, CA 91109, USA

B. T. Draine
Department of Astrophysical Sciences, Princeton University, Princeton, NJ 08544, USA

(Dated: November 29, 2016)
Draft version November 29, 2016

ABSTRACT

Interstellar iron in the form of metallic iron nanoparticles may constitute a component of the interstellar dust. We compute the stability of iron nanoparticles to sublimation in the interstellar radiation field, finding that iron clusters can persist down to a radius of $\simeq 4.5\,\text{Å}$, and perhaps smaller. We employ laboratory data on small iron clusters to compute the photoelectric yields as a function of grain size and the resulting grain charge distribution in various interstellar environments, finding that iron nanoparticles can acquire negative charges particularly in regions with high gas temperatures and ionization fractions. If $\gtrsim 10\%$ of the interstellar iron is in the form of ultrasmall iron clusters, the photoelectric heating rate from dust may be increased by up to tens of percent relative to dust models with only carbonaceous and silicate grains.

1. INTRODUCTION

More than 95% of interstellar iron is depleted from the gas phase (Jenkins 2009), suggesting that iron is the largest elemental contributor to the interstellar dust mass after oxygen and carbon (e.g. Draine 2011, Table 23.1). Silicate grains provide a possible reservoir for the iron in the form of interstellar pyroxene ($Mg_xFe_{1-x}SiO_3$) or olivine ($Mg_{2x}Fe_{2-2x}SiO_4$) analogues. However, the shape and strength of the $9.7\,\mu$m silicate feature in extinction suggest that the silicate material is magnesium-rich rather than iron-rich (Poteet et al. 2015) and therefore that a substantial fraction ($\sim$70%) of the interstellar iron is in other forms such as iron oxides (e.g. Fe_3O_4, Cox 1990; Jones 1990; Henning et al. 1995; Draine & Hensley 2013), iron sulfides (e.g. FeS, Bradley 1994; Köhler et al. 2014), or metallic iron (Schalen 1965; Chlewicki & Laureijs 1988).

Metallic Fe inclusions have been found in interplanetary dust particles (Bradley 1994), lunar soil samples (Keller & McKay 1997), and, most recently, in putative interstellar grains collected in the Solar System (Westphal et al. 2014; Altobelli et al. 2016). Thus, metallic iron is a particularly compelling candidate material whether in the form of inclusions in larger grains or, as we focus on in this work, free-flying nanoparticles.

Because metallic Fe has no infrared or UV resonances, IR and UV spectroscopy does not place limits on the fraction of interstellar Fe that is metallic. Paerels et al. (2001) concluded that X-ray spectroscopy near the Fe L_2 and L_3 edges agreed better with metallic Fe than with Fe oxides, but Valencic & Smith (2013) conclude that the fits are not particularly good, and other Fe compounds can fit the $L_{2,3}$ edges nearly as well. A large fraction of interstellar Fe could be in metallic Fe nanoparticles without having noticeably affected the interstellar extinction curve (see Figure 13 of Draine & Hensley 2013).

Nevertheless, metallic iron can greatly impact observed dust properties. If metallic Fe is present in the form of inclusions, it could contribute to the alignment of interstellar dust grains: alignment by magnetic dissipation in spinning grains, as proposed by Davis & Greenstein (1951), could be faster if ferromagnetic materials are present (Jones & Spitzer 1967; Duley 1978; Hoang & Lazarian 2016a). Both free-flying and included Fe nanoparticles emit thermal magnetic dipole radiation at submillimeter and millimeter wavelengths (Draine & Lazarian 1999; Draine & Hensley 2013), and such grains have been invoked to explained the observed excess submillimeter-millimeter emission in the Small Magellanic Cloud (Draine & Hensley 2012). Magnetic dipole emission from aligned metallic iron grains or from iron inclusions in aligned grains is polarized orthogonally to the electric dipole emission from non-magnetic grains. Thus, the presence of metallic Fe grains could dramatically affect the polarized Galactic dust spectral energy distribution (SED) by effectively "diluting" the polarized electric dipole emission. The *Planck* satellite has observed that the polarization fraction of the dust emission declines with increasing wavelength (Planck Collaboration et al. 2015), consistent with predictions from models of magnetic dust (Draine & Hensley 2013).

In addition to affecting far-infrared dust emission and polarization, stochastically-heated free-flying Fe nanoparticles may contribute significantly to the infrared dust emission near $20\,\mu$m. Photoelectric heating is dominated by the smallest grains (e.g. Bakes & Tielens 1994; Weingartner & Draine 2001), and so a population of iron nanoparticles may contribute to interstellar heating. Finally, Fe nanoparticles may be responsible for part or all of the so-called anomalous microwave emission (AME) peaking near $\sim$30 GHz either through thermal magnetic dipole emission (Draine & Lazarian 1999; Draine & Hensley 2013) or rotational emission (Hoang & Lazarian 2016b). In a separate study (Hensley & Draine 2016, in prep.), we examine the mid-infrared emission from Fe nanoparticles undergoing stochastic heating, and

brandon.s.hensley@jpl.nasa.gov

from this we obtain upper limits on the fraction of the observed AME that could be due to rotational emission from Fe nanoparticles.

Given the potential importance of Fe nanoparticles as a component of interstellar dust, in this work we investigate the thermodynamic and photoelectric properties of these grains. In Section 2, we discuss the heating and sublimation rate of Fe nanoparticles and compute a minimum grain size that is stable to sublimation; in Section 3, we discuss the collisional charging and photoelectric emission from these grains and compute the resulting grain charge distribution as a function of grain size; in Section 4, we quantify the contribution of these grains to the photoelectric heating in various interstellar environments; finally, we summarize our principal conclusions in Section 5.

2. GRAIN HEATING AND SUBLIMATION

2.1. *Destruction by Desorption*

2.1.1. *Thermal Energy vs. T*

The experimentally-measured heat content of bulk Fe as measured by Desai (1986) is shown in Figure 1. At low temperature ($T < 800\,\mathrm{K}$) the internal energy per atom of bulk Fe is well-approximated by a Debye model plus an electronic heat capacity:

$$\frac{E_\infty(T)}{k} = 9\Theta_\mathrm{D}\int_0^1 \frac{x^3 dx}{\exp(x\Theta_\mathrm{D}/T)-1} + \frac{\gamma}{2}T^2 \quad , \quad (1)$$

where the Debye temperature $\Theta_\mathrm{D} = 415\,\mathrm{K}$, and $\gamma = 6\times10^{-4}\,\mathrm{K}^{-1}$. Equation 1 is plotted in Figure 1. It fits the experimental data well for $T < 300\,\mathrm{K}$, but at higher temperatures the experimental heat capacity is larger than given by Equation 1. We use the laboratory data in Figure 1 to relate the internal energy E to the temperature T.

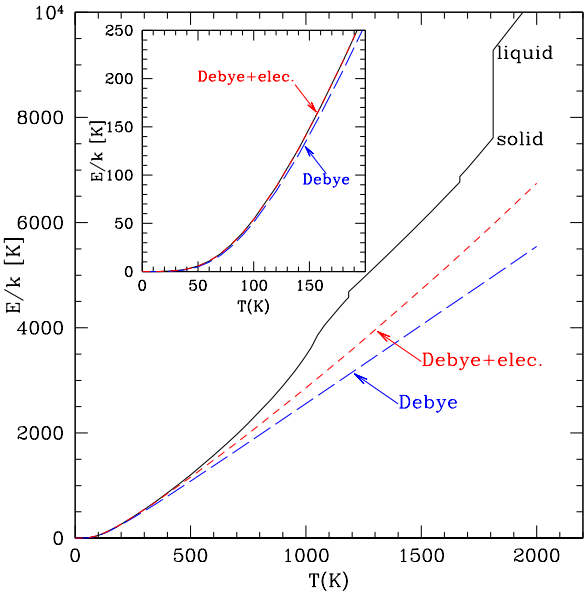

FIG. 1.— E/k, where E is the heat of formation per atom of bulk Fe, relative to $T = 0\,\mathrm{K}$, from Desai (1986). The discontinuities at $T = 1185\,\mathrm{K}$ and $1667\,\mathrm{K}$ are the $\alpha-\gamma$ and $\gamma-\delta$ phase transitions, and the larger discontinuity at $T = 1811\,\mathrm{K}$ is the solid-liquid phase transition. The dashed red line is the Debye model plus electronic specific heat (Equation 1).

2.1.2. *Vapor Pressure*

The saturation vapor pressure of bulk Fe is approximated by (see Figure 2):

$$p_\mathrm{sat}(T) = 4.80\times10^{12}T_3\exp(-47.18/T_3)\,\mathrm{erg\,cm^{-3}} \quad (2)$$

where $T_3 \equiv T/10^3\,\mathrm{K}$, so that the saturation concentration is

$$c_1^\mathrm{sat} = \frac{p_\mathrm{sat}}{kT} = 3.48\times10^{25}\exp(-47.18/T_3)\,\mathrm{cm^{-3}} \quad . \quad (3)$$

The saturation vapor pressure for monomers in equilibrium with clusters of Fe_n atoms will be greater than the bulk value, because the binding energy per atom is lowered by surface curvature (i.e., surface free energy). In LTE, the rate per surface area of sublimation of monomers from a cluster of n atoms is estimated to be (Guhathakurta & Draine 1989)

$$R_n(T) \approx \alpha_{n-1}c_1^\mathrm{sat}\left(\frac{kT}{2\pi m}\right)^{1/2}\exp\left(\frac{\theta_\infty/T}{(n-1)^{1/3}}\right) \quad , \quad (4)$$

where α_{n-1} is the sticking coefficient for Fe atoms colliding with Fe_{n-1}, and

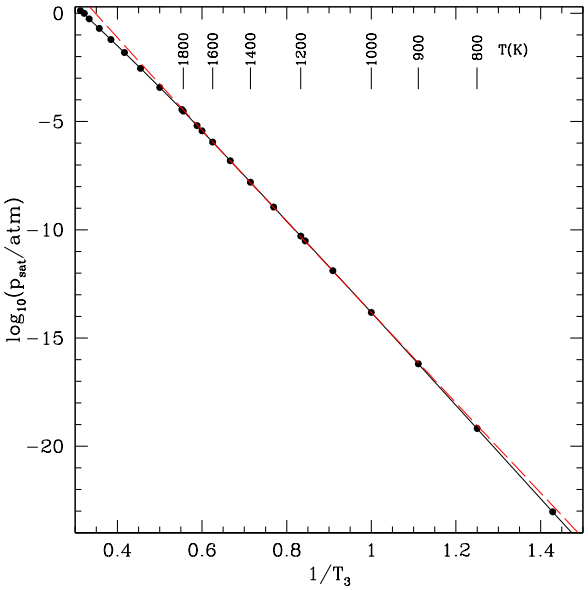

FIG. 2.— Solid curve: experimental saturation vapor pressure of Fe (Desai 1986). Dashed: Equation 2.

$$\theta_\infty = \left(\frac{32\pi}{3}\right)^{1/3}\left(\frac{m}{\rho}\right)^{2/3}\frac{\sigma}{k} \quad , \quad (5)$$

where σ is the surface free energy. Experimental data on molten Fe is approximated by $\sigma \approx [1918 - 0.43(T/\,\mathrm{K} - 1811)]\,\mathrm{erg\,cm^{-2}}$ (Kasama et al. 1983). The surface free energy of solid bcc Fe at low temperatures is estimated to be $\sigma \approx 2410\,\mathrm{erg\,cm^{-2}}$ (Tyson & Miller 1977). For the temperatures $T \approx 1200\,\mathrm{K}$ of interest for Fe sublimation,

we will take $\sigma \approx 2200\,\mathrm{erg\,cm^{-2}}$, corresponding to

$$\theta_\infty \approx 2.67\times10^4\,\mathrm{K} \quad . \tag{6}$$

A cluster Fe_n has surface area $A_n \approx 2.51\times10^{-15}n^{2/3}\,\mathrm{cm^2}$. If we take $\alpha_n \approx 0.5$, then in LTE the rate coefficient for $\mathrm{Fe}_n \rightarrow \mathrm{Fe}_{n-1} + \mathrm{Fe}$ is

$$k_{n\rightarrow n-1}^{\rm LTE} \approx 6.71\times10^{14}n^{2/3}T_3^{1/2} \times \exp\left[-\frac{47.18}{T_3}+\frac{26.7}{T_3}(n-1)^{-1/3}\right]\,\mathrm{s^{-1}} \quad . \tag{7}$$

The effective energy B required to liberate one Fe atom from a cluster Fe_n is

$$B \approx k\left[47180\,\mathrm{K}-\frac{26700\,\mathrm{K}}{(n-1)^{1/3}}\right] = \left[4.07-2.30(n-1)^{-1/3}\right]\,\mathrm{eV} \quad . \tag{8}$$

A cluster containing a fixed energy E is *not* in LTE with a heat bath. Fluctuations must concentrate an energy $> B$ into a single vibrational mode to break the bond holding one of the surface Fe atoms to the rest of the cluster. The sublimation rate is suppressed below the LTE rate by a factor that can be estimated using "quantum RRK" theory for unimolecular reaction rates (Robinson & Holbrook 1972). The suppression factor is estimated to be (Guhathakurta & Draine 1989)

$$S_n = \left(1+\frac{1}{\gamma}\right)^b \frac{\Gamma(\gamma f+1)}{\Gamma(\gamma f+f)}\frac{\Gamma(\gamma f+f-b)}{\Gamma(\gamma f+1-b)} \quad , \tag{9}$$

where $f = 3(n-2)$ is the number of vibrational degrees of freedom of the Fe_n cluster,

$$\gamma \equiv \frac{E/f}{\hbar\omega_0} \tag{10}$$

is internal energy per mode divided by $\hbar\omega_0$, and

$$b \equiv \frac{B}{\hbar\omega_0} \tag{11}$$

is the binding energy divided by the vibrational quantum. We take $\hbar\omega_0 = (3/4)k\Theta_{\rm D}$, the mean mode energy for a 3-dimensional Debye spectrum. Thus, consider a nanoparticle Fe_n undergoing stochastic heating and cooling, with P_E being the probability of being found with internal energy E. We take the sublimation rate to be

$$\left(\frac{dn}{dt}\right)_E = -\sum_E P_E S_n(E)\times k_{n\rightarrow n-1}^{\rm LTE}(T_E) \quad , \tag{12}$$

where $S_n(E)$ is given by Equation 9, the "effective temperature" T_E is the temperature where bulk Fe has the same mean energy per degree of freedom as the cluster with energy E:

$$E_\infty(T_E) = \frac{E}{n-2} \quad , \tag{13}$$

and the dimensionless quantities b, f, and γ are

$$b = 144.6 - 71.1(n-1)^{-1/3} \tag{14}$$

$$f = 3(n-2) \tag{15}$$

$$\gamma = \frac{E/f}{(3/4)k\Theta_{\rm D}} \quad . \tag{16}$$

2.2. *Distribution Function for Internal Energy*

The internal energy of a cluster varies with time, with upward spikes following photon absorption, and downward transitions as the result of thermal emission (i.e., spontaneous decays). We divide the range of likely internal energies into a finite number (499) of energy bins. The time-averaged probability P_j of finding a Fe_n cluster in energy bin E_j is obtained by finding the steady state solution P_i satisfying

$$0 = \sum_{j\neq i} T_{ji}P_i \qquad 1 = \sum_j P_j \tag{17}$$

where the transition matrix T_{ji} is the probability per unit time of a cluster in state i making a transition $i \rightarrow j$. Transition matrix elements T_{ji} for downward transitions were calculated with infrared emission treated as discrete transitions (Draine & Li 2001). Upward T_{ji} were calculated using photoabsorption cross sections derived from the dielectric function for metallic Fe from Draine & Hensley (2013, Appendix B).

Examples of energy distribution functions are shown in Figure 3 for Fe nanoparticles heated by the Mathis et al. (1983) interstellar radiation field. The results shown in Figure 3 were obtained assuming that the only cooling process is thermal emission of photons.

The distribution functions in Figure 3 all show a dramatic drop at $E/hc = 1.097\times10^5\,\mathrm{cm^{-1}}$, corresponding to $E = 13.60\,\mathrm{eV}$, because the starlight spectrum is assumed to be cut off above this energy. Following a photon absorption, a cluster cools very rapidly and is likely to be in the ground vibrational state (or very close to it) when the next photon absorption event occurs. Even for a cluster with as many as 355 atoms, the probability of having an appreciable internal energy $E > 1\,\mathrm{eV}$ is $\sim 10^{-3}$, but this is enough for the internal distribution P_E to begin to extend noticeably above the 13.6 eV cutoff (see Figure 3a). To illustrate what grain temperatures are reached during the "thermal spikes" due to photon heating events, Figure 3b shows $dP/d\ln E$ vs. the grain "temperature" T_E.

Grains with $n \lesssim 50$ reach peak temperatures $T > 10^3\,\mathrm{K}$. While the melting temperature of bulk Fe is $T = 1811\,\mathrm{K}$, melting point depression due to small particle effects can lower the melting point below 900 K (Duan et al. 2007). Thus, hot Fe_n clusters may be liquid at their highest temperatures.[1] The energy required to effect these phase transitions would, for the same heat capacities, slightly decrease the peak temperature attained by these grains; however, whether the grain is solid or liquid does not affect our estimate of the evaporation rate from the grain's surface (Equation 4). Note that the saturation vapor pressure for bulk Fe is continuous across the solid-liquid phase transition (see Figure 2).

[1] Of course, the notion of "melting" is itself not well-defined for small atomic clusters.

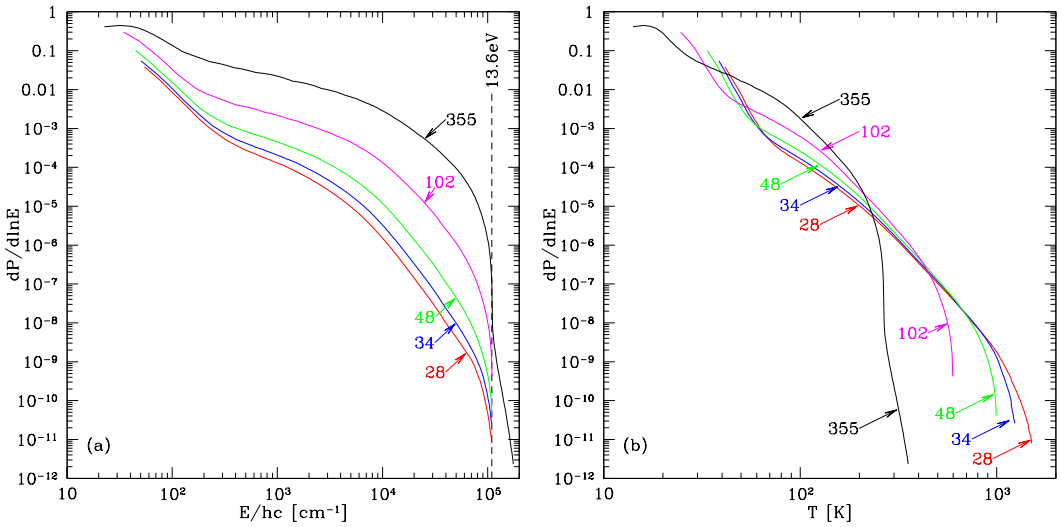

FIG. 3.— Energy distribution function for Fe_n nanoparticles vs. energy (left) and temperature (right). Curves are labelled by number n of Fe atoms in the nanoparticle.

In the diffuse cold neutral medium (CNM), only about 1% of the Fe is in the gas phase: $n(Fe^+) \approx 1\times10^{-5}\,cm^{-3}$, and thermal Fe^+ ions would collide with a neutral Fe_{30} cluster at a rate (Draine & Sutin 1987)

$$\left(\frac{dn}{dt}\right)_{coll} \approx 3\times10^{-9}\,cm^3\,s^{-1}n(Fe^+) \approx 3\times10^{-14}\,s^{-1} \quad (18)$$

corresponding to a very long mass doubling time $\sim 3\times10^7\,yr$. Growth by accretion from the gas is very slow. Replenishment of the mass in very small clusters is instead probably dominated by fragmentation of larger grains.

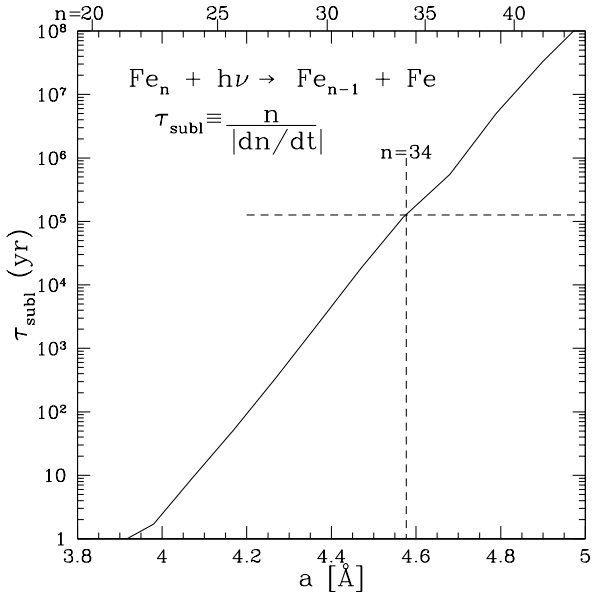

FIG. 4.— Lifetime against thermal sublimation for Fe nanoparticles heated by the interstellar radiation field.

For each grain size, we have calculated the thermal sublimation rate using Equation 12. The resulting timescales for thermal sublimation are shown, as a function of grain size, in Figure 4. We see from Figure 4 that a Fe_{34} nanoparticle has a lifetime against destruction by thermal sublimation $\tau_{subl} \approx 10^5\,yr$, and this lifetime drops to only $\sim 10^4\,yr$ for Fe_{30}. Thus, unless important cooling processes have been neglected, we expect that Fe nanoparticles in the ISM will contain $n \geq 34$ atoms, i.e., will have radii $a > 4.5\,Å$ (see Equation 30).

From Figure 3 we see that clusters with $n = 34$ and $n = 48$ have very similar temperature distribution functions for $T < 1000\,K$. The $n = 34$ cluster has a much shorter lifetime, however, because its temperature distribution function extends up to $\sim 1300\,K$. From this we see that the sublimation that limits the sizes of Fe nanoparticles takes place at temperatures $T \approx 1200 \pm 200\,K$. Note that our empirical fit to the saturation vapor pressure closely reproduces experimental data (for bulk Fe) over this range.

2.3. *Other Cooling Processes*

2.3.1. *Sublimation Cooling?*

The above calculation of P_E assumed that the only cooling process for a cluster is thermal emission. Of course, sublimation of an Fe atom ($Fe_n \rightarrow Fe_{n-1}+Fe$, Equation 8) involves breaking a bond, and thus leaves the Fe_{n-1} cluster in a cooler state from which a second sublimation event will be extremely unlikely. We have seen above that sublimation is only important for $T > 10^3\,K$. At $T > 10^3\,K$, the radiative cooling time for a Fe nanoparticle is $t_{cool} \sim 10^{-2}\,s$. The total rate of starlight absorption events for a cluster Fe_n is

$$R_\star \approx 5\times10^{-9}Un\,s^{-1} \quad (19)$$

where the dimensionless factor U is the intensity of the starlight relative to the Mathis et al. (1983) estimate for the local interstellar radiation field. The rate of sublimation is

$$R_{sub} = 3\times10^{-13}n\left(\frac{\tau_{subl}}{10^5\,yr}\right)^{-1}\,s^{-1} \quad . \quad (20)$$

The number of sublimations per photon absorption

$$\frac{R_{\rm subl}}{R_\star} \approx 6\times10^{-5}U^{-1}\left(\frac{\tau_{\rm subl}}{10^5\,{\rm yr}}\right)^{-1} \ll 1 \quad . \tag{21}$$

Only a very small fraction of the photon absorption events result in a sublimation, even for grains that are near our estimated minimum cutoff (sublimation lifetime $\tau_{\rm subl} \approx 10^5\,{\rm yr}$). Neglecting sublimation cooling, this means that only a fraction $(R_{\rm subl}/R_\star)$ of the sublimations would occur in thermal spikes with two independent sublimations. Thus our neglect of sublimation cooling has resulted in only a slight overestimate of the sublimation rate.

2.3.2. *Thermionic Emission Cooling?*

A hot grain can also lose energy by emitting electrons – the process known as "thermionic emission".

A neutral Fe_n nanoparticle can emit an electron

$$Fe_n + \Delta E \rightarrow Fe_n^+ + e^- \tag{22}$$

if the energy ΔE exceeds the ionization potential IP. Yang & Knickelbein (1990) have measured ionization potentials for Fe_n with $5 \le n \le 90$ (see Figure 6), and the experimental value of the ionization potential for $n = 34$ is 5.06 eV. Thus the cost of ejecting an electron from Fe_{34} is greater than the binding energy $B \approx 3.4\,{\rm eV}$ of a Fe atom (see Equation 8). The ionization potential for Fe_n^+ cations is even greater, and thermionic emission is even less likely. For a Fermi velocity of order $1000\,{\rm km\,s^{-1}}$, the trial frequency would be of order $4\times10^{16}\,{\rm Hz}$, or a factor of 4000 higher than the vibrational frequency. For a 1200 K grain near its sublimation temperature, the 1.66 eV difference between the grain's binding energy and ionization potential corresponds to an exponential suppression factor of $\exp(\text{-}1.66\,{\rm eV}/k\times1200\,{\rm K}) = 10^{-7}$. Thus, for $T \approx 1200\,{\rm K}$ the frequency of thermionic emission will be only $\sim 4\times10^{-4}$ that of thermal sublimation of Fe, and can be neglected.

Under interstellar conditions, there is a significant probability that a Fe nanoparticle can be negatively charged: Fe_n^-. The energy to remove an electron from an Fe_n^- anion is equal to the "electron affinity" EA of the neutral Fe_n. Electron affinities have been determined from photoelectron spectroscopy of iron clusters (Wang et al. 2000, see Figure 7), with $EA \approx 2.5\,{\rm eV}$ for $n \approx 34$. This is smaller than the estimated Fe atom binding energy $B \approx 3.4\,{\rm eV}$ for $n \approx 34$. It therefore seems likely that a hot Fe_n^- will cool by emitting an electron before an Fe atom is sublimed.

Under conditions typical of the cold neutral medium (CNM, see Figure 10), we expect the majority of the Fe_n to be either neutral or positively charged. Accordingly, it does not appear that cooling by thermionic emission will significantly reduce the rate of sublimation of Fe atoms from Fe_n clusters in the CNM. However, in highly-ionized environments where collisions with electrons are frequent, the grains can acquire negative charges (see Figure 10). In these environments, thermionic emission may allow the grains to persist to somewhat smaller radii.

2.4. *Desorption of H*

H atoms arrive at the surface of an uncharged Fe_n nanoparticle at a rate

$$\begin{aligned}\dot{N}({\rm H\,arrival}) &= n({\rm H})\left(\frac{8kT}{\pi m_{\rm H}}\right)^{1/2}\pi a^2 \\ &= 2.9\times10^{-8}\left(\frac{n({\rm H})}{30\,{\rm cm^{-3}}}\right)\left(\frac{T}{10^2\,{\rm K}}\right)^{1/2}\left(\frac{n}{34}\right)^{2/3} \quad ,\end{aligned} \tag{23}$$

with somewhat higher collision rates (because of the induced-dipole interaction) for clusters that are charged. This is much higher than the rate of Fe desorptions:

$$\dot{N}({\rm Fe\,sublimation}) = 1.1\times10^{-11}\left(\frac{n}{34}\right)\left(\frac{10^5\,{\rm yr}}{\tau_{\rm subl}}\right)\,{\rm s^{-1}} \quad . \tag{24}$$

A fraction $f_{\rm chem}$ of arriving H atoms will stick to the grain and be chemisorbed. Chemisorption of H atoms on bcc Fe has been studied experimentally and theoretically. The tightest binding appears to be for the Fe(110) surface, with a binding energy $2.86\pm0.05\,{\rm eV/atom}$ (Jiang & Carter 2003). Note that H_2 formation is energetically unfavorable relative to two H atoms bound to Fe. Only after monolayer coverage is achieved would H_2 formation take place on the surface.

The estimated binding energy $B_{\rm H} \approx 2.86\,{\rm eV}$ of a chemisorbed H atom on Fe (100) is less than the estimated binding energy $B \approx 3.4\,{\rm eV}$ for an Fe atom. Thus a hot Fe_n cluster with chemisorbed H will desorb H atoms more rapidly than Fe. Loss of one or more H atoms will cool the cluster enough that no Fe atoms will be desorbed during that thermal spike.

For Fe_n clusters with submonolayer coverage of H, desorption of adsorbed H atoms could potentially cool the cluster and reduce the loss of Fe atoms. The effects of adsorbed H on the temperature probability distribution for Fe_n clusters, and on their survival in the ISM, will be the subject of future investigation. However, at this time it seems evident that desorption of H will lead to a significant reduction in the minimum size of the Fe cluster that can survive in the diffuse ISM, and we will therefore consider cluster sizes as small as $n = 25$ ($a = 4.0\,{\rm Å}$).

2.5. *Other Destruction Processes*

While we have emphasized destruction due to heating from ambient starlight, other mechanisms may also limit the lifetimes of iron nanoparticles in the ISM. In this section, we discuss the effects of X-ray absorption and reactive sputtering.

Upon absorption of a $\sim 1\,{\rm keV}$ X-ray, an iron nanoparticle would likely undergo photoelectric emission of an L shell electron, followed by emission of several Auger electrons. Some of the remaining energy could conceivably evaporate one or more Fe atoms from the grain surface. However, for an X-ray density of $10^{-8}\,{\rm cm^{-3}}$ (see Draine 2011, Figure 12.1) and an absorption efficiency $Q_{\rm abs} \simeq 1.4\times10^{-2}$ for a 1 nm metallic iron grain, an X-ray absorption would occur only every 3×10^5 years.

Chemisputtering, particularly due to H and O atoms, is another another potential destruction pathway. The surface chemistry, including the effects of vacuum ultraviolet radiation, is poorly understood – it is conceivable, for

TABLE 1
IDEALIZED ISM PHASES

	CNM	WNM	WIM
$n_{\rm H}\,({\rm cm}^{-3})$	30	0.4	0.1
$T_g\,({\rm K})$	100	6000	8000
$x_{\rm H} \equiv n({\rm H}^+)/n_{\rm H}$	0.0012	0.1	0.99
$x_{\rm C} \equiv n({\rm C}^+)/n_{\rm H}$	0.0003	0.0003	0.001

NOTE. — Hydrogen number density $n_{\rm H}$, gas temperature T_g, H^+ abundance $x_{\rm H}$, and C^+ abundance $x_{\rm C}$ adopted for the cold neutral medium (CNM), warm neutral medium (WNM), and warm ionized medium (WIM) following Draine & Lazarian (1998).

instance, that impinging O atoms may be chemisorbed, forming an oxide coating on the Fe nanoparticle, but also plausible that such chemisorbed O atoms could be removed via chemisputtering by impinging H atoms. Whether interstellar chemistry is capable of maintaining a population of pure metallic Fe nanoparticles is beyond the scope of this work, particularly in light of the present uncertainties. Rather, we focus instead on the observable consequences should such a population exist, and compute the lifetime of such a grain exposed to the interstellar radiation field.

3. GRAIN CHARGE DISTRIBUTION

The grain charge distribution is the result of statistical equilibrium between the processes of collisional charging and photoelectric emission. Denoting the electron and ion collision rates as $J_{\rm e}(Z,a)$ and $J_{\rm i}(Z,a)$, respectively, and the rate of photoelectric emission $J_{\rm pe}(Z,a)$, in statistical equilibrium we have

$$\left[J_{\rm i}(Z,a) + J_{\rm pe}(Z,a)\right] f_a(Z) = J_{\rm e}(Z+1,a) f_a(Z+1) \quad , \tag{25}$$

where $f_a(Z)$ denotes the probability of a grain with radius a having charge Z. To compute these rates for iron nanoparticles, we follow closely the treatment of Weingartner & Draine (2001) for carbonaceous and silicate grains, adapting it where necessary to the case of metallic iron. We refer the interested reader to that work for a more thorough explication of the physics and derivations of the results employed here. The charge distribution is calculated for three idealized ISM phases– the cold neutral medium (CNM), warm neutral medium (WNM), and warm ionized medium (WIM). We adopt the parameterizations of these media suggested by Draine & Lazarian (1998) and presented in Table 1.

3.1. *Collisional Charging*

The rate of sticking collisions of a species i (in this work, we will consider electrons as well as H^+ and C^+ ions) with a spherical grain of radius a and charge Z is given by

$$J(Z,a) = n_i s_i(Z) \left(\frac{8kT_g}{\pi m_i}\right)^{1/2} \pi a^2 \widetilde{J}(\tau_i,\nu_i) \quad , \tag{26}$$

where n_i is the number density of species i, m_i is the mass of species i, and T_g is the gas temperature. The function $s_i(Z)$ is the sticking efficiency of species i onto a grain of charge Z, and the function $\widetilde{J}(\tau,\nu)$ accounts for the effect of Coulomb focusing. It is given by (Draine & Sutin 1987)

$$\widetilde{J}(\tau,\nu) \simeq \begin{cases} 1 + \left(\dfrac{\pi}{2\tau}\right)^{1/2}, & \nu = 0 \\ \left[1 - \dfrac{\nu}{\tau}\right]\left[1 + \left(\dfrac{2}{\tau - 2\nu}\right)^{1/2}\right], & \nu < 0 \\ \left[1 + (4\tau + 3\nu)^{-1/2}\right]^2 \exp\left(-\theta_\nu/\tau\right), & \nu > 0, \end{cases} \tag{27}$$

where $\tau_i = akT_g/q_i^2$ is the "reduced temperature," $\nu_i = Ze/q_i$, q_i is the charge of species i, and

$$\theta_\nu(\nu > 0) \simeq \frac{\nu}{1 + \nu^{-1/2}} \quad . \tag{28}$$

The grain composition enters into the charging rates only through the sticking efficiency $s_i(Z)$. Unfortunately, there is a dearth of laboratory data constraining the sticking efficiencies of iron nanoparticles, so we adopt the empirical treatment of Weingartner & Draine (2001). For ions, we assume $s_{\rm ion} = 1$. For electrons, we adopt

$$s_e(Z > Z_{\rm min}) = 0.5\left(1 - e^{-a/l_e}\right) \quad , \tag{29}$$

where l_e is the electron escape length (see Section 3.2) and $Z_{\rm min}$ is the minimum grain charge (see Equation 47). For $Z = Z_{\rm min}$, the grain will autoionize following an electron collision, and so $s_e(Z_{\rm min}) = 0$. Note that in the absence of experimental data, we have ignored suppression of the sticking efficiency in the smallest grains (cf. Weingartner & Draine 2001, Equation 28).

In Figure 5, we plot the collisional charging rates for iron nanoparticles as a function of size in each of the idealized ISM environments detailed in Table 1.

3.2. *Photoelectric Emission*

We will now compute the rate of photoelectric emission of iron nanoparticles as a function of grain size and charge. Consider spherical iron nanoparticles with mass density $\rho = 7.87\,{\rm g\,cm}^{-3}$. The number of iron atoms n in a cluster with radius a can be approximated by

$$n = 352\left(\frac{a}{10\,{\rm \AA}}\right)^3 \quad . \tag{30}$$

The ionization potential (IP, also referred to as the ionization energy) can be calculated classically with the "spherical drop model" (SDM) in which the cluster is modeled as a conducting sphere. In the SDM, the energy required to move an electron from the surface of a sphere of charge Z is given by

$${\rm IP}_{\rm SDM}(Z) = W + \left(Z + \frac{1}{2}\right)\frac{e^2}{a} \quad , \tag{31}$$

where W is the bulk work function of the material. For metallic iron, $W = 4.5\,{\rm eV}$ (Eastman 1970). In contrast to the predictions of the spherical drop model, experimental data indicate very little evolution of IP between

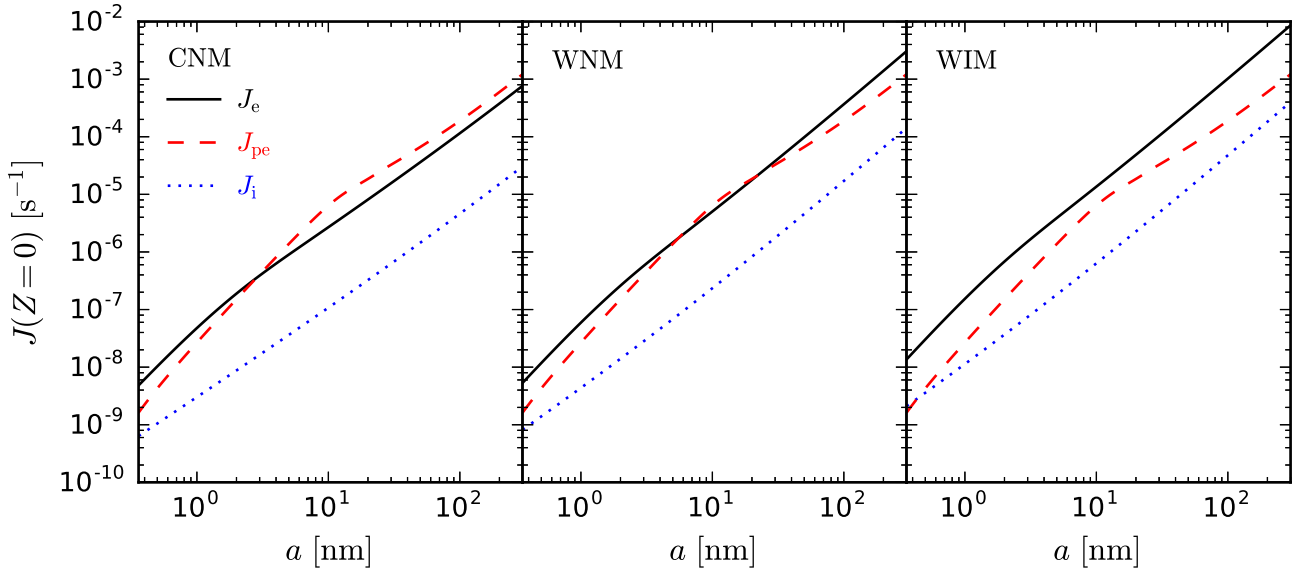

FIG. 5.— The rate of collisional charging due to electrons (black solid) and ions (blue dotted) and the rate photoelectric charging (red dashed) are plotted as a function of grain size for CNM (left), WNM (middle) and WIM (right) environments for neutral iron grains. The relatively inefficient photoelectric yield of these grains can cause electrons to accumulate on the grains leading to preferentially negative grain charges.

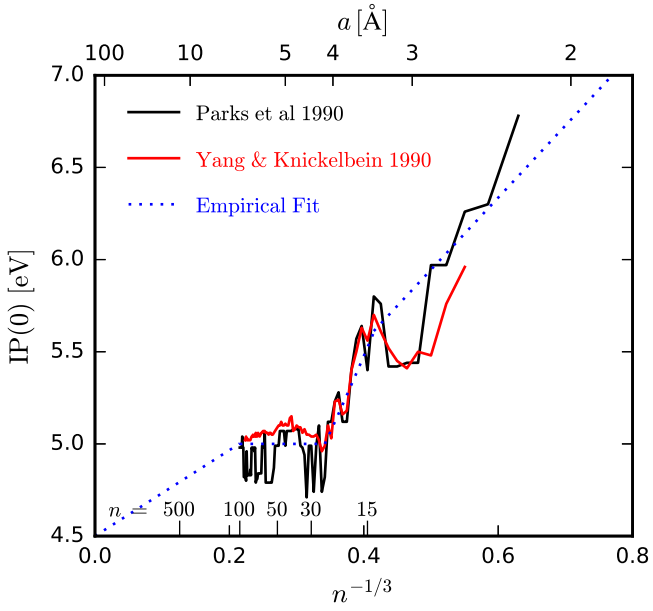

FIG. 6.— The ionization potential (IP) for clusters of n iron atoms as determined by Parks et al. (1990) (black) and Yang & Knickelbein (1990) (red). Agreement between the two sets of experimental data is good; however, the data are in sharp disagreement with the spherical drop model. We overlay our empirical fit to the experimental data (blue dotted).

$30 \lesssim n \lesssim 100$ (Parks et al. 1990; Yang & Knickelbein 1990). We plot these data in Figure 6.

We approximate IP(0) with an empirical fit to the experimental data (see Figure 6) based on a modification of Equation 31. For $Z \geq 0$, we take

$$\mathrm{IP}(Z \geq 0) = \begin{cases} 3.99\,\mathrm{eV} + (Z+0.38)\dfrac{e^2}{a}, & n < 14 \\ 2.22\,\mathrm{eV} + (Z+0.80)\dfrac{e^2}{a}, & 14 \leq n < 25 \\ 5.00\,\mathrm{eV} + Z\dfrac{e^2}{a}, & 25 \leq n < 100 \\ W + (Z+0.23)\dfrac{e^2}{a}, & n \geq 100 \end{cases} \quad (32)$$

Grains with $Z < 0$ have "extra" electrons in their molecular orbitals. The energy required to ionize a grain of charge $Z < 0$ is equal to the energy gained by adding an electron to a grain of charge $Z+1$. This latter quantity is called the "electron affinity" EA, and so $\mathrm{IP}(Z<0) = \mathrm{EA}(Z+1)$. In the case of iron, which should not have an energy band gap, the EA is also expected to follow the SDM.

Wang et al. (1995) employed photoelectron spectroscopy to measure the EA for iron clusters with $3 \leq n \leq 34$ atoms and found that EA scales with $n^{-1/3}$ as expected from the SDM above $n \simeq 20$. We find good numerical agreement with their results, as shown in Figure 7, by adopting

$$\mathrm{EA}(Z) = \begin{cases} 5.18\,\mathrm{eV} + (Z-0.69)\dfrac{e^2}{a}, & n < 13 \\ 2.20\,\mathrm{eV} + Z\dfrac{e^2}{a}, & 13 \leq n < 24 \\ W + (Z-0.66)\dfrac{e^2}{a}, & n \geq 24 \end{cases} \quad (33)$$

which, with Equation 32, fully specifies IP as a function of a and Z.

Let us define $h\nu_{\mathrm{pet}}$ as the threshold photon energy for photoionization. For grains with $Z \geq -1$, this energy

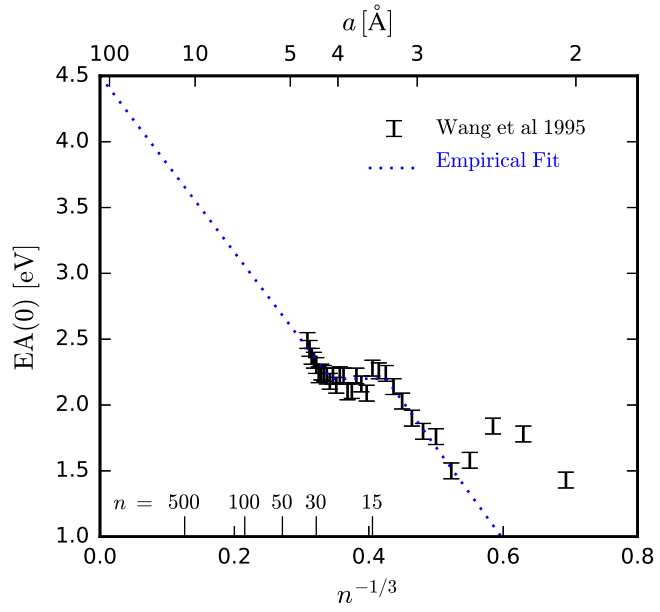

FIG. 7.— The electron affinity for neutral iron clusters of n atoms as measured by Wang et al. (1995). We overlay our model (Equation 33) which extrapolates the experimental data to the bulk limit with a modified form of the spherical drop model (blue dotted line).

is simply equal to the energy difference IP required to move an electron from the grain to infinity. However, when $Z < -1$ the grain repels the escaping electron, so that it necessarily arrives at infinity with kinetic energy $\geq E_{\rm min}$. Thus the minimum photon energy to eject the electron must be

$$h\nu_{\rm pet}(Z,a) = \begin{cases} {\rm IP}(Z,a), & Z \geq -1 \\ {\rm IP}(Z,a) + E_{\rm min}(Z,a), & Z < -1 \end{cases} \quad (34)$$

We adopt the $E_{\rm min}$ prescription of van Hoof et al. (2004):

$$E_{\rm min} = \theta_\nu \left(|Z+1|\right) \left[1 - 0.3 \left(\frac{a}{10\,{\rm Å}}\right)^{-0.45} |Z+1|^{-0.26}\right] \quad , \quad (35)$$

where θ_ν is given by Equation 28.

We now quantify the expected number of electrons yielded by a photon of energy $h\nu > h\nu_{\rm pet}$. Consider first the yield y_0' of electrons that escape the grain surface but may or may not escape to infinity. We employ the model

$$y_0'\left(h\nu, Z, a\right) = y_0\left(\Theta\right) y_1\left(h\nu, a\right) \quad , \quad (36)$$

where $y_0(\Theta)$ primarily governs the frequency-dependence of the yield in the limit of bulk material, y_1 quantifies the yield enhancement due to geometrical effects, and Θ is a parameter defined by

$$\Theta = \begin{cases} h\nu - h\nu_{\rm pet} + (Z+1)\, e^2/a, & Z \geq 0 \\ h\nu - h\nu_{\rm pet}, & Z < 0 \end{cases} \quad . (37)$$

y_1 can be approximated by (Draine 1978)

$$y_1 = \left(\frac{\beta}{\alpha}\right)^2 \frac{\alpha^2 - 2\alpha + 2 - 2e^{-\alpha}}{\beta^2 - 2\beta + 2 - 2e^{-\beta}} \quad , \quad (38)$$

where $\alpha = a/l_a + a/l_e$, $\beta = a/l_a$, l_e is the electron escape length, and l_a is the photon attenuation length. For a material with complex refractive index $m\left(\lambda\right)$, l_a is given by

$$l_a = \frac{\lambda}{4\pi\,{\rm Im}\left(m\right)} \quad . \quad (39)$$

We employ the complex refractive index for metallic Fe from Draine & Hensley (2013).

The electron escape length l_e is the mean free path of an electron to inelastic scattering and is a parameter in models for the photoelelectric yield of grains as well as for the sticking efficiency (see Equation 29). The energy-dependence of l_e has been measured for a range of materials and is generally found to decrease with electron energy at low energy, have a minimum between 10 and 100 eV above the Fermi surface, then increase to high energies (Seah & Dench 1979). As experimental data are sparse and as the minimum is coincident with energies of astrophysical interest, some previous studies have adopted an energy-independent $l_e = 10\,{\rm Å}$ (Bakes & Tielens 1994; Weingartner & Draine 2001). Kimura (2016) instead adopts the empirical prescription of Seah & Dench (1979) for the case of pure elements:

$$l_e = 143 \left(\frac{E}{\rm eV}\right)^{-2} + 0.054 \left(\frac{E}{\rm eV}\right)^{1/2} \ {\rm nm} \quad , \quad (40)$$

where here E is the energy above the Fermi level. This prescription yields $l_e = 16\,{\rm Å}$ at $E = 10\,{\rm eV}$. Given the current state of experimental uncertainty, as well as the rough agreement between approaches in the regime of interest, we opt for the simpler energy-independent treatment with $l_e = 10\,{\rm Å}$.

Previous studies (Bakes & Tielens 1994; Weingartner & Draine 2001) have determined y_0 by matching model predictions to experimental data at some fixed grain size and charge. In Figure 8, we plot the bulk photoelectric yield of metallic iron as measured by Quemerais et al. (1985). We find that we can obtain reasonable agreement with the experimental data by adopting:

$$y_0 = \frac{2.1 \times 10^{-3} \left(\Theta/W\right)^5}{1 + 6.8 \times 10^{-3} \left(\Theta/W\right)^5} \quad , \quad (41)$$

with Θ given by Equation 37.

Finally, we define y_2 as the fraction of electrons that emerge from the grain surface that escape to infinity. We follow Weingartner & Draine (2001) in assuming a parabolic distribution of electron energies, yielding

$$y_2 = \begin{cases} E_{\rm high}^2 \left(E_{\rm high} - 3E_{\rm low}\right) / \left(E_{\rm high} - E_{\rm low}\right)^3, & Z \geq 0 \\ 1, & Z < 0, \end{cases} \quad (42)$$

where $E_{\rm low} = -(Z+1)e^2/a$ and $E_{\rm high} = h\nu - h\nu_{\rm pet}$. Thus, the photoelectric yield Y is given by

$$Y(h\nu, Z, a) = y_2 \min\left(y_0', 1\right) \quad . \quad (43)$$

In Figure 9 we plot the yield for iron nanoparticles of

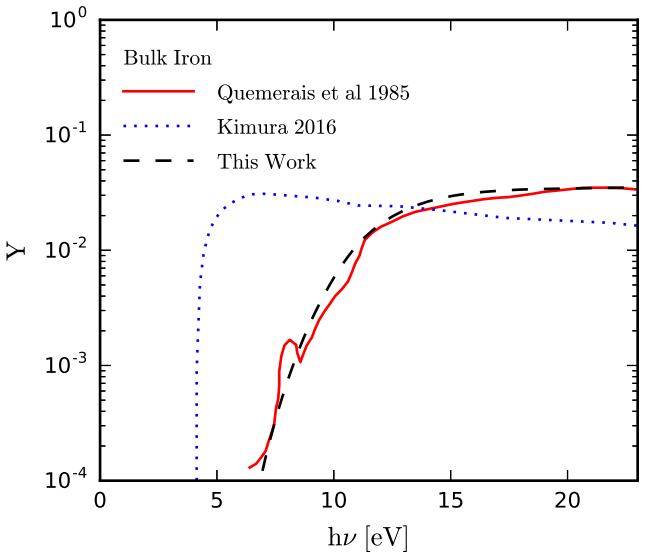

FIG. 8.— The photoelectric yield Y for bulk iron as measured by Quemerais et al. (1985) (red solid line) and for our model with $a = 100\,\mathrm{nm}$ (black dashed line). We also plot the model of Kimura (2016) (blue dotted), but note that, unlike our model, it was not explicitly calibrated on the experimental data.

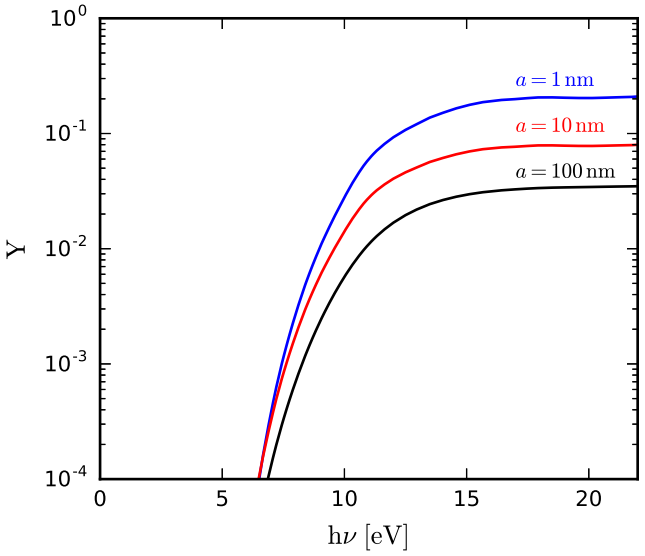

FIG. 9.— The photoelectric yield of neutral iron nanoparticles of radius 1, 10, and 100 nm. The enhancement of the photoelectric yield due to small particle effects saturates at roughly $a = 1\,\mathrm{nm}$, so the energy-dependent photoelectric yield of the $a = 1\,\mathrm{nm}$ grains is also representative of smaller grains.

radius 1, 10, and 100 nm. The yield for particles with $a < 1\,\mathrm{nm}$ is similar to that of 1 nm grains.

As a final step in computing the photoelectric charging rate $J_{\rm pe}$, we consider the photodetachment of electrons above the valence band for grains with $Z < 0$. The photodetachment threshold energy $h\nu_{\rm pdt}$ is

$$h\nu_{\rm pdt} = \mathrm{EA}\left(Z+1,a\right) + E_{\rm min}\left(Z,a\right) \quad . \tag{44}$$

We follow Weingartner & Draine (2001) in adopting

$$\sigma_{\rm pdt} = \frac{-1.2\times10^{-17}Zx}{\left(1+x^2/3\right)^2}\ \mathrm{cm}^2 \tag{45}$$

for the photodetachment cross section $\sigma_{\rm pdt}$, where $x \equiv \left(h\nu - h\nu_{\rm pdt}\right)/3\,\mathrm{eV}$.

For a spherical grain of radius a with absorption efficiency $Q_{\rm abs}\left(\nu\right)$ in a radiation field with specific energy density $u_\nu\left(\nu\right)$, the photoemission rate is

$$J_{\rm pe}\left(Z,a\right) = \pi a^2 \int_{\nu_{\rm pet}}^{\infty} \mathrm{d}\nu\, Y\, Q_{\rm abs}\, \frac{cu_\nu}{h\nu} + \int_{\nu_{\rm pdt}}^{\infty} \mathrm{d}\nu\, \sigma_{\rm pdt}\, \frac{cu_\nu}{h\nu} \quad . \tag{46}$$

We adopt the absorption efficiencies of metallic Fe computed by Draine & Hensley (2013) and the starlight energy density spectrum of Mathis et al. (1983). The rate of photoelectric emission is compared to the collisional charging rates in Figure 5 for iron grains of various sizes in CNM, WNM, and WIM environments.

3.3. *Charge Distribution*

Once the collisional charging rates and photoelectric emission rates have been computed, Equation 25 can be solved recursively after a minimum and maximum grain charge ($Z_{\rm min}$ and $Z_{\rm max}$, respectively) have been determined.

If an electron is added to a grain of sufficiently negative potential, the grain will autoionize. Denoting the threshold autionization threshold potential $U_{\rm ait}$, we have

$$Z_{\rm min} = 1 + \left\lfloor \frac{U_{\rm ait}}{e/a} \right\rfloor \quad , \tag{47}$$

where $\lfloor\rfloor$ is the floor function. As graphite and iron have similar work functions (4.4 and 4.5 eV, respectively), we adopt the $U_{\rm ait}$ derived for carbonaceous grains by Weingartner & Draine (2001):

$$\frac{-U_{\rm ait}}{\mathrm{V}} = 3.9 + 0.12\left(a/\mathrm{\AA}\right) + 2\left(\mathrm{\AA}/a\right) \quad . \tag{48}$$

A grain achieves its maximum charge when its ionization potential becomes larger than the maximum photon energy of the ambient radiation field $h\nu_{\rm max}$, here taken to be 13.6 eV. Thus,

$$Z_{\rm max} = \begin{cases} \left\lfloor 0.62 + \frac{a}{e^2}\left(h\nu_{\rm max} - 3.99\,\mathrm{eV}\right)\right\rfloor, & n < 14 \\ \left\lfloor 0.20 + \frac{a}{e^2}\left(h\nu_{\rm max} - 2.22\,\mathrm{eV}\right)\right\rfloor, & 14 \le n < 25 \\ \left\lfloor 1 + \frac{a}{e^2}\left(h\nu_{\rm max} - 5\,\mathrm{eV}\right)\right\rfloor, & 25 \le n < 100 \\ \left\lfloor 0.77 + \frac{a}{e^2}\left(h\nu_{\rm max} - W\right)\right\rfloor, & n \ge 100. \end{cases} \tag{49}$$

In Figure 10 we present the final charge distributions of iron nanoparticles in the CNM, WNM, and WIM for grain sizes of 5, 10, 50, and 100 Å.

Perhaps the most striking feature of the grain charge distributions is the tendency of iron nanoparticles to acquire *negative* charge, in contrast to the typically positively-charged carbonaceous and silicate grains (see Weingartner & Draine 2001, Figure 10). This is due largely to the relatively inefficient photoelectric yield of the iron grains.

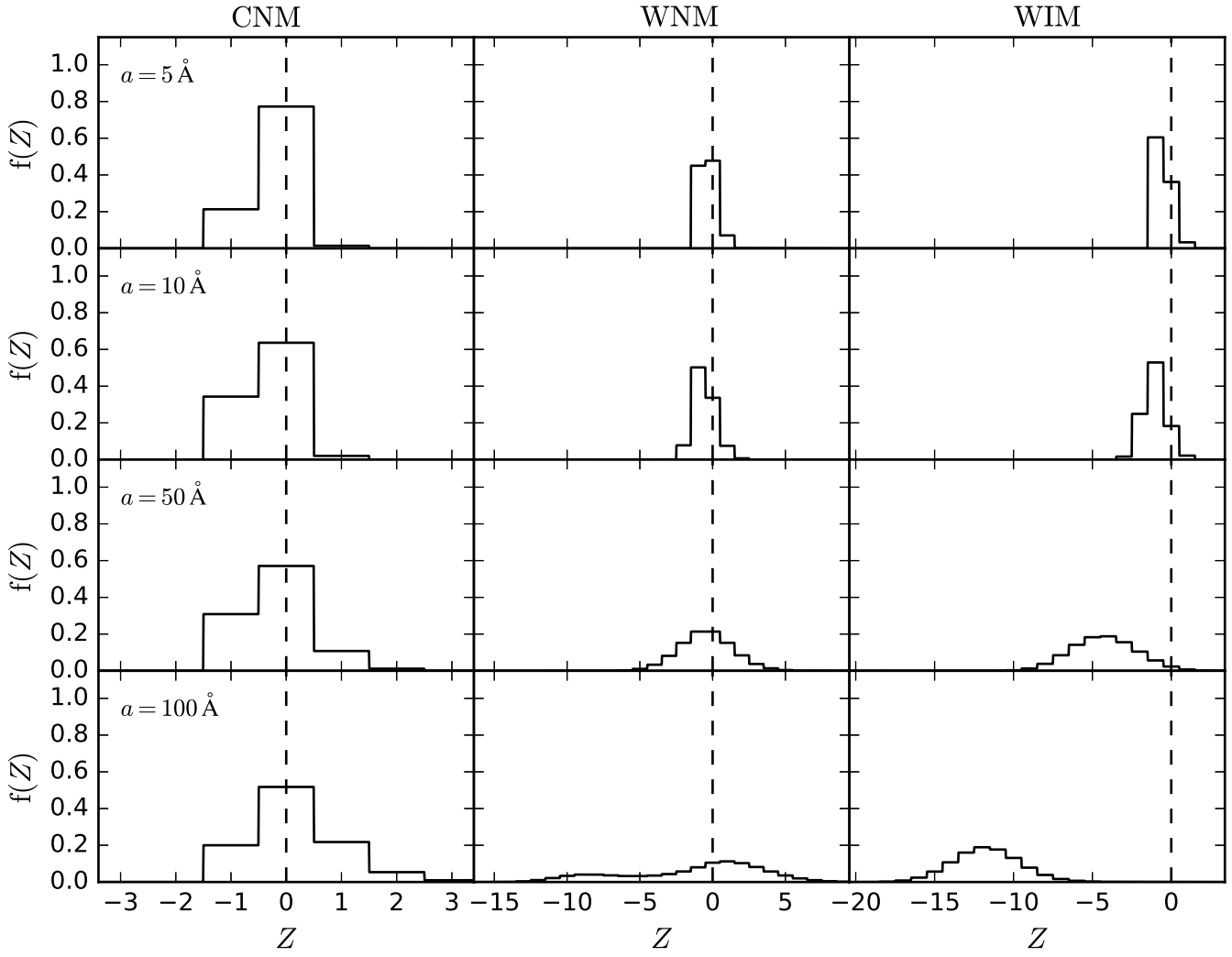

FIG. 10.— The grain charge distribution for 5 (top row), 10 (second row), 50 (third row), and 100 Å (bottom row) iron nanoparticles in the CNM (left column), WNM (middle column), and WIM (right column). Of particular note is the tendency for these grains to be charged to *negative* potentials, particularly in the WNM and WIM due to their relatively low photoelectric emission rates (see Figure 5).

4. PHOTOELECTRIC HEATING

Energetic electrons photoelectrically ejected from grains serve as a major heating source of the ambient interstellar gas. In this section, we quantify the potential contribution of iron nanoparticles to the total photoelectric heating from dust. We again follow closely Weingartner & Draine (2001).

As discussed above, electrons are liberated from grains via photoemission of valence electrons and the photodetachment of electrons above the valence band. Let $\Gamma'_{\rm pe}$ be the total heating rate per grain from photoelectric emission, which can be computed for iron nanoparticles from Weingartner & Draine (2001, Equations 38 - 40) by employing the model of photoelectric emission from iron grains presented in this work.

Grains also capture electrons and thereby remove energy from the gas, and so the total heating rate per grain is lessened by the energy removal rate $\Lambda'_{\rm gr}$ (see Weingartner & Draine 2001, Equation 42). The total gas heating efficiency per grain ϵ_Γ is defined by

$$\epsilon_\Gamma = \frac{\Gamma'_{\rm pe} - \Lambda'_{\rm gr}}{\pi a^2 c \int u_\nu \, Q_{\rm abs} \, {\rm d}\nu} \quad . \tag{50}$$

We plot ϵ_Γ for iron nanoparticles in various interstellar environments in Figure 11. As expected due to the enhancement of the photoelectric yield in small particles, the smallest grains are most effective at heating the gas. The smallest iron nanoparticles are only slightly less efficient at heating the gas than silicate grains and approximately a factor of two less efficient than carbonaceous grains as computed by Weingartner & Draine (2001).

It is not known how much of the interstellar iron is in the form of free-flying iron nanoparticles. Adopting a solid-phase interstellar iron abundance of 41 ppm (Bensby et al. 2005; Lodders et al. 2009; Jenkins 2009) and a fraction $Y_{\rm Fe}$ of that iron in the form of free-flying iron nanoparticles, we assume a log-normal size distribution for $a > a_{\rm min}$:

$$\frac{1}{n_{\rm H}} \frac{{\rm d}n_{\rm Fe}}{{\rm d}a} = \frac{A}{a} \exp\left\{ -\frac{1}{2} \left[\frac{\ln\left(a/a_0\right)}{\widetilde{\sigma}} \right]^2 \right\} \quad , \tag{51}$$

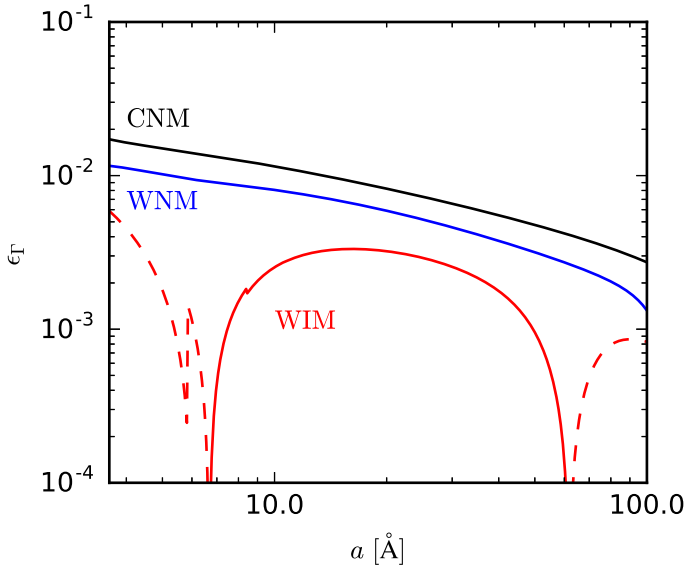

FIG. 11.— The photoelectric heating efficiency ϵ_Γ as a function of grain size in the CNM, WNM, and WIM. For very small and large grains in the WIM, collisional cooling is more efficient than photoelectric heating, giving these grains a net *cooling* effect on the gas ($\epsilon_\Gamma < 0$ is indicated with a dashed line). As was found for carbonaceous and silicate grains, photoelectric heating from iron grains is dominated by the smallest grains.

where the parameters a_0 and $\widetilde{\sigma}$ determine the peak size and width of the size distribution. A is a normalization constant given by

$$A = \frac{3}{(2\pi)^{3/2}} \frac{\exp\left(-4.5\widetilde{\sigma}^2\right)}{a_0^3 \rho \widetilde{\sigma}} \times \frac{m_{\rm Fe} b_{\rm Fe}}{1 + \mathrm{erf}\left[3\widetilde{\sigma}/\sqrt{2} + \ln\left(a_0/a_{\rm min}\right)/\widetilde{\sigma}\sqrt{2}\right]} \quad (52)$$

for $a > a_{\rm min}$ and zero otherwise, where $\rho = 7.87\,{\rm g\,cm^{-3}}$ is the grain mass density, $m_{\rm Fe} = 9.27 \times 10^{-23}\,{\rm g}$ is the mass of an iron atom, and $b_{\rm Fe} = 41 Y_{\rm Fe} \times 10^{-6}$ is the number of Fe atoms per H consumed by this grain population. We adopt $a_0 = a_{\rm min} = 4.5\,{\rm Å}$ and $\widetilde{\sigma} = 0.3$ as an illustrative case that roughly maximizes the photoelectric heating of this population by concentrating the grain mass at the smallest viable sizes.

With this size distribution, we compute the total photoelectric heating rate per H nucleon per Habing flux via

$$\frac{\Gamma_{\rm tot}}{G n_{\rm H}} = \int \frac{\Gamma'_{\rm pe} - \Lambda'_{\rm gr}}{G} \frac{1}{n_{\rm H}} \frac{{\rm d}n_{\rm Fe}}{{\rm d}a}\, {\rm d}a \quad (53)$$

where the adopted radiation field of Mathis et al. (1983) has G = 1.13.

This population of iron nanoparticles yields a total heating rate per H nucleon per Habing flux of $2 \times 10^{-26} Y_{\rm Fe}$ and $1 \times 10^{-26} Y_{\rm Fe}\,{\rm erg\,s^{-1}\,H^{-1}}$ in the CNM and WNM, respectively. In contrast, Weingartner & Draine (2001) found heating rates of 6×10^{-26} and $3 \times 10^{-26}\,{\rm erg\,s^{-1}\,H^{-1}}$ in the CNM and WNM, respectively, for a combination of carbonaceous and silicate grains. In the WIM, the iron grains provide a small source of *cooling* at the level of $2 \times 10^{-27} Y_{\rm Fe}\,{\rm erg\,s^{-1}\,H^{-1}}$, but this is small relative to the heating rates that have been estimated for photoionization from starlight or photoelectric heating from dust ($\sim 10^{-25} - 10^{-24}\,{\rm erg\,s^{-1}\,H^{-1}}$ Mathis 2000; Weingartner & Draine 2001).

Iron nanoparticles therefore appear able to make a minor but non-negligible contribution to the total photoelectric heating provided some ($Y_{\rm Fe} \gtrsim 10\%$) of the interstellar iron exists in the form of small, free-flying particles.

5. CONCLUSIONS

The abundance of solid phase iron in the interstellar medium suggests that iron nanoparticles may be a substantial component of interstellar dust. Such particles could contribute to the interstellar extinction and to the infrared emission. Magnetic dipole emission and rotational emission from these grains could potentially contribute importantly to the Galactic dust SED at submillimeter and microwave wavelengths. In this work, we have investigated the physics of these grains, focusing on their thermodynamics, photodestuction, and charging. Our principal conclusions are as follows:

1. Bare Fe_n nanoparticles are unstable to photodestuction in the interstellar radiation field below $n = 34$ ($a = 4.5\,{\rm Å}$). In the presence of H atoms, Fe nanoparticles will be partially hydrogenated, and cooling by thermal desorption of H atoms will allow the Fe cores to survive down to smaller sizes, perhaps $n = 25$ ($a = 4.0\,{\rm Å}$) in the diffuse ISM.

2. Due to a photoelectric yield lower than that of either carbonaceous or silicate grains, iron grains tend to be charged to negative potentials particularly in environments such as the WNM or WIM where the electron collision rate is high.

3. If $\gtrsim 10\%$ of the interstellar iron is in the form of metallic iron nanoparticles, these grains could increase the photoelectric heating from dust by up to tens of percent relative to models with only carbonaceous and silicate dust.

4. A large population of interstellar metallic iron nanoparticles can be considered a viable component of interstellar dust without having an unphysically large impact on interstellar heating.

The results presented in this work rest, where possible, upon available laboratory data. However, for materials of size and composition of astrophysical interest, the data are sparse. Laboratory measurements of the photoelectric yield of small iron clusters, as well as carbonaceous and silicate materials, would be of particular use, as would additional measurement of the ionization potential and electron affinity for larger iron clusters ($n > 100$).

We thank referee J. Nuth and a second anonymous referee for helpful comments. BTD acknowledges support from NSF grant AST-1408723. The research was carried out in part at the Jet Propulsion Laboratory, California Institute of Technology, under a contract with the National Aeronautics and Space Administration.

REFERENCES

Altobelli, N., Postberg, F., Fiege, K., et al. 2016, Science, 352, 312
Bakes, E. L. O., & Tielens, A. G. G. M. 1994, ApJ, 427, 822
Bensby, T., Feltzing, S., Lundström, I., & Ilyin, I. 2005, A&A, 433, 185
Bradley, J. P. 1994, Science, 265, 925
Chlewicki, G., & Laureijs, R. J. 1988, A&A, 207, L11
Cox, P. 1990, A&A, 236, L29
Davis, Jr., L., & Greenstein, J. L. 1951, ApJ, 114, 206
Desai, P. D. 1986, Journal of Physical and Chemical Reference Data, 15, 967
Draine, B. T. 1978, ApJS, 36, 595
—. 2011, Physics of the Interstellar and Intergalactic Medium (Princeton, NJ: Princeton University Press)
Draine, B. T., & Hensley, B. 2012, ApJ, 757, 103
—. 2013, ApJ, 765, 159
Draine, B. T., & Lazarian, A. 1998, ApJ, 508, 157
—. 1999, ApJ, 512, 740
Draine, B. T., & Li, A. 2001, ApJ, 551, 807
Draine, B. T., & Sutin, B. 1987, ApJ, 320, 803
Duan, H., Ding, F., Rosén, A., et al. 2007, Chemical Physics, 333, 57
Duley, W. W. 1978, ApJ, 219, L129
Eastman, D. E. 1970, Phys. Rev. B, 2, 1
Guhathakurta, P., & Draine, B. T. 1989, ApJ, 345, 230
Henning, T., Begemann, B., Mutschke, H., & Dorschner, J. 1995, A&AS, 112, 143
Hensley, B. S., & Draine, B. T. 2016, In prep
Hoang, T., & Lazarian, A. 2016a, ArXiv e-prints, arXiv:1605.02828
—. 2016b, ApJ, 821, 91
Jenkins, E. B. 2009, ApJ, 700, 1299
Jiang, D. E., & Carter, E. A. 2003, Surface Science, 547, 85
Jones, A. P. 1990, MNRAS, 245, 331
Jones, R. V., & Spitzer, Jr., L. 1967, ApJ, 147, 943
Kasama, A., McLean, A., Miller, W. A., Z., M., & Ward, M. J. 1983, Canadian Metallurgical Quarterly, 22, 9
Keller, L. P., & McKay, D. S. 1997, Geochim. Cosmochim. Acta, 61, 2331
Kimura, H. 2016, MNRAS, 459, 2751
Köhler, M., Jones, A., & Ysard, N. 2014, A&A, 565, L9
Lodders, K., Palme, H., & Gail, H.-P. 2009, Landolt Börnstein, 44
Mathis, J. S. 2000, ApJ, 544, 347
Mathis, J. S., Mezger, P. G., & Panagia, N. 1983, A&A, 128, 212
Paerels, F., Brinkman, A. C., van der Meer, R. L. J., et al. 2001, ApJ, 546, 338
Parks, E. K., Klots, T. D., & Riley, S. J. 1990, J. Chem. Phys., 92, 3813
Planck Collaboration, Ade, P. A. R., Alves, M. I. R., et al. 2015, A&A, 576, A107
Poteet, C. A., Whittet, D. C. B., & Draine, B. T. 2015, ApJ, 801, 110
Quemerais, A., Seignac, A., Priol, M., & Lefevre, J. 1985, in Astrophysics and Space Science Library, Vol. 119, IAU Colloq. 85: Properties and Interactions of Interplanetary Dust, ed. R. H. Giese & P. Lamy, 329–333
Robinson, P. J., & Holbrook, K. A. 1972, Unimolecular Reactions (New York: Wiley)
Schalen, C. 1965, PASP, 77, 409
Seah, M. P., & Dench, W. A. 1979, Surface and Interface Analysis, 1, 2
Tyson, W. R., & Miller, W. A. 1977, Surface Science, 62, 267
Valencic, L. A., & Smith, R. K. 2013, ApJ, 770, 22
van Hoof, P. A. M., Weingartner, J. C., Martin, P. G., Volk, K., & Ferland, G. J. 2004, MNRAS, 350, 1330
Wang, L.-S., Cheng, H.-S., & Fan, J. 1995, J. Chem. Phys., 102, 9480
Wang, L.-S., Li, X., & Zhang, H.-F. 2000, Chemical Physics, 262, 53
Weingartner, J. C., & Draine, B. T. 2001, ApJS, 134, 263
Westphal, A. J., Stroud, R. M., Bechtel, H. A., et al. 2014, Science, 345, 786
Yang, S., & Knickelbein, M. B. 1990, J. Chem. Phys., 93, 1533